Journal of Biomedical Optics

SPIEDigitalLibrary.org/jbo

Towards pH-sensitive imaging of small animals with photon-counting difference diffuse fluorescence tomography

Jiao Li
Xin Wang
Xi Yi
Limin Zhang
Zhongxing Zhou
Huijuan Zhao
Feng Gao

SPIE

Towards pH-sensitive imaging of small animals with photon-counting difference diffuse fluorescence tomography

Jiao Li,[a] Xin Wang,[a] Xi Yi,[a] Limin Zhang,[a,b] Zhongxing Zhou,[a,b] Huijuan Zhao,[a,b] and Feng Gao[a,b]
[a]Tianjin University, College of Precision Instruments and Optoelectronics Engineering, Tianjin 300072, China
[b]Tianjin Key Laboratory of Biomedical Detecting Techniques and Instruments, Tianjin 300072, China

Abstract. The importance of cellular pH has been shown clearly in the study of cell activity, pathological feature, and drug metabolism. Monitoring pH changes of living cells and imaging the regions with abnormal pH-values, *in vivo*, could provide invaluable physiological and pathological information for the research of the cell biology, pharmacokinetics, diagnostics, and therapeutics of certain diseases such as cancer. Naturally, pH-sensitive fluorescence imaging of bulk tissues has been attracting great attentions from the realm of near infrared diffuse fluorescence tomography (DFT). Herein, the feasibility of quantifying pH-induced fluorescence changes in turbid medium is investigated using a continuous-wave difference-DFT technique that is based on the specifically designed computed tomography-analogous photon counting system and the Born normalized difference image reconstruction scheme. We have validated the methodology using two-dimensional imaging experiments on a small-animal-sized phantom, embedding an inclusion with varying pH-values. The results show that the proposed approach can accurately localize the target with a quantitative resolution to pH-sensitive variation of the fluorescent yield, and might provide a promising alternative method of pH-sensitive fluorescence imaging in addition to the fluorescence-lifetime imaging. [DOI: 10.1117/1.JBO.17.9.096011]

Keywords: diffuse fluorescence tomography; pH-sensitive detection; quantitative reconstruction; photon counting; computed tomography-analogous scanning.

Paper 12280 received May 4, 2012; revised manuscript received Jul. 28, 2012; accepted for publication Aug. 1, 2012; published online Sep. 14, 2012.

1 Introduction

The cellular pH plays a significant role in biological functions such as cell metabolism, multidrug resistance, ion transport, and muscle contraction.[1] It has been well established, that cellular dysfunction often has intimate connection with abnormal pH-values in organelles. Thus, monitoring cellular pH changes can provide physiological and pathological information for studying the cell biology and pharmacokinetics. Also, many common diseases such as cancer, ischemic stroke, Alzheimer's disease, atherosclerotic plaques, and others are associated with increased metabolic activity and hypoxia resulting in a lower pH condition.[2,3] Imaging the disease regions where pH-value is becoming unusual, as compared with normal tissue, could offer more information about localization and progression of diseases.[4]

A number of methods are available to measure cellular pH, such as nuclear magnetic resonance (NMR) spectrum, pH microelectrodes, weak acid/ base indicator, pH-sensitive dyes and fluorescent probes.[5–8] In comparison with other pH measurement methods, the technique of imaging pH-sensitive fluorescent probes is extremely sensitive, and could provide high spatial and temporal observation of pH changes. As a simple implementation of this technique, the two-dimensional (2-D) ratio-metric photographic approach constructs an image by calculating ratio of the reflected signals, at the emission wavelength to those at the excitation wavelength, and can overcome quantitative limitation of the absolute optical pH measurement. Although this planar imaging approach has gained wide popularity in measuring pH dynamics of living cells, it lacks in depth-resolved and quantitative capabilities, for *in vivo* applications, due to the diffusive nature of photons in tissue.[9,10]

Contrast to the planar imaging technique, near infrared (NIR) DFT combines advantages of high sensitivity of fluorescent probe and quantitative performance of the model-based diffuse optical tomography (DOT) and has been emerging as a powerful *in vivo* small animal imaging tool.[9–11] DFT aims at visualizing interior cellular and molecular events through recovering biodistributions of the fluorescent parameters, yield and/or lifetime, inside intact tissues from fluorescence signals measured on the tissue boundary, and can be accomplished in principle with three commonly used modes of DOT instrumentation which are continuous-wave (CW),[11–13] frequency-domain (FD)[14] and time-domain (TD).[15–18] For small animal applications, however, a FD system is not commonly used because the small tissue size to be imaged requires a modulation frequency higher than 300 MHz, incurring an impractical, costly expense of the instrumentation. As a result, CW instruments are often developed to achieve the yield imaging while TD ones are used to, additionally, obtain lifetime information.[16]

Normally, both the fluorescence yield and lifetime could be pH-sensitive by choosing an appropriate fluorescence probe. Although much effort has been made in acquiring the concentration-independent lifetime images of turbid medium through

Address all correspondence to: Feng Gao, Tianjin University, College of Precision Instrument and Optoelectronics Engineering, Weijinlu Avenue #92, Tianjin 300072, China. Tel: +86-22-27403801; Fax: +86-22-27403801; E-mail: gaofeng@tju.edu.cn; or Jiao Li, E-mail: jiaoli@tju.edu.cn

0091-3286/2012/$25.00 © 2012 SPIE

TD DFT technique, its performance has been rather limited in terms of the reconstruction artifacts and quantitative accuracy.[16] This is primarily due to the relatively low disease-to-normal contrast of the lifetime property and the unknown background condition. On the other hand, imaging of the yield parameter, i.e., the product of the quantum-efficiency and concentration of the fluorophore, has proven to be very robust and, therefore, could provide a reliable way of monitoring cellular pH changes inside tissues. Furthermore, the yield-imaging instrument, with ultralow noise characteristics and ultrahigh dynamic range, could be cost-effectively achieved with a CW photon-counting technique which allows for an improved quantification of pH-related signal and an extended imaging size to rats, even to human organs.[19]

This study addresses the potential of CW difference-DFT scheme to quantitatively disclose pH-sensitive fluorescence variation in turbid medium. To maximize quantitative assessment to variation of the fluorescence yield with environmental pH-value, we have developed a photon-counting system with computed tomography (CT)-analogous scanning mode and utilized the Born normalized difference image reconstruction algorithm. The experimental validations were performed on a rat-sized cylindrical phantom, with a Cy5.5 fluorescent inclusion, under a variety of pH environments for three target-to-background concentration contrasts to simulate the different stages of cancer development. The results were compared with those obtained using the ratio-metric photographic technique.[20]

2 Methods

2.1 *System*

Among CW techniques for diffuse light imaging, charge-coupled-device (CCD) camera and photo-multipliter-tube (PMT)-based photon counting are most commonly employed.[9–14,16] Comparatively, the former provides a parallelized data acquisition scheme for fast, high density spatial sampling, but has limited dynamic range that might be problematic for imaging large-size subject with weak targets, while the latter is so far the most sensitive and offers exceptional dynamic range, but has to be improved for its high-density sampling capacity. It is demonstrated, that improved performance of the data acquisition can be achieved by introduction of the noncontact scanning scheme for both the photon-counting and CCD modes, resulting in evident modification of the spatial resolution and quantitative accuracy.[21–23]

Our experimental studies are performed with a CT-analogous photon counting system, as shown in Fig. 1. The system uses

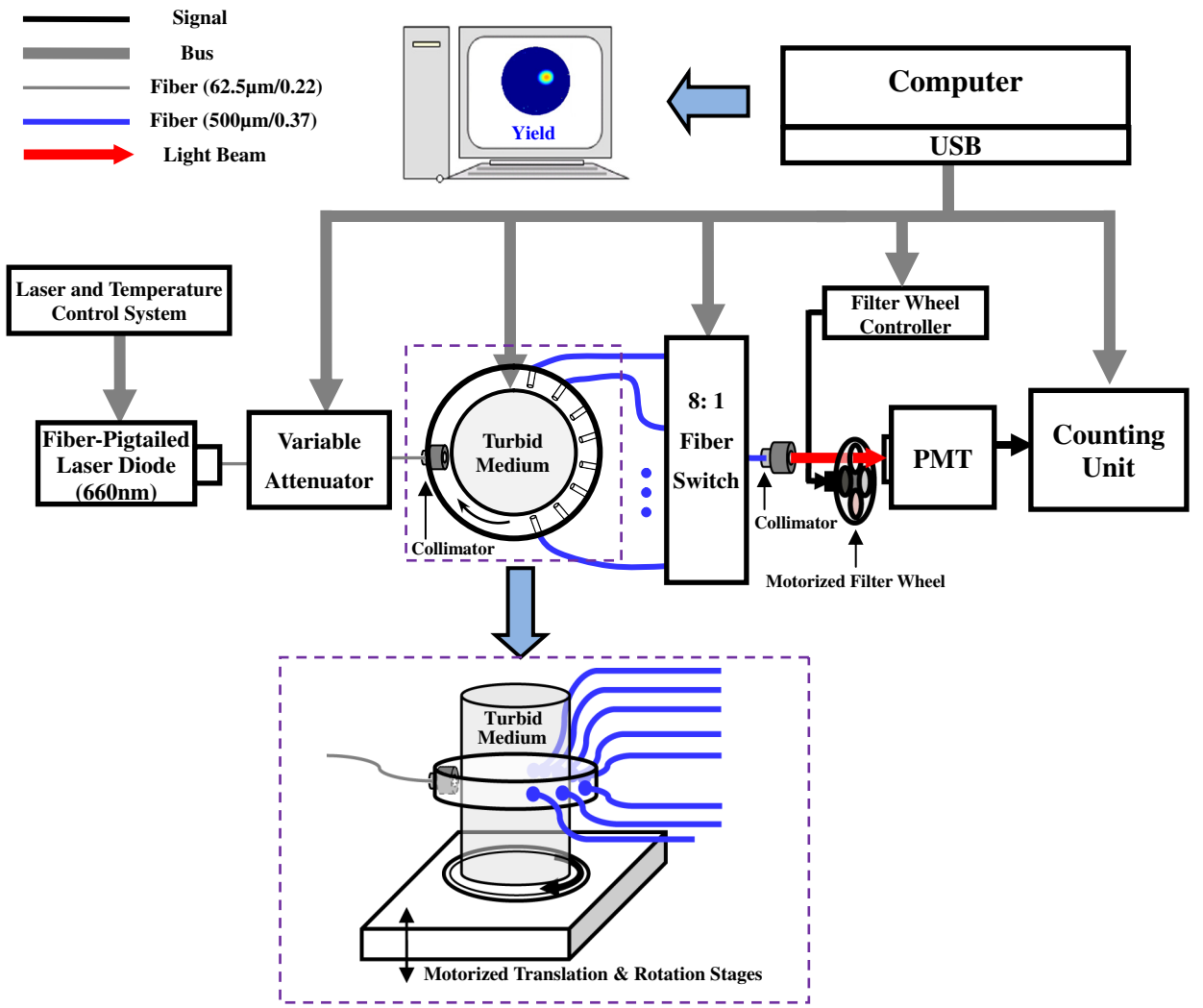

Fig. 1 The CW DFT experimental setup using a CT-analogous photon counting system.

a diode laser set consisting of a 660-nm fiber-tailed diode (LPS-660-FC, Thorlabs), specially, for Cy5.5 dye with its peak excitation and emission wavelengths at 670 and 710 nm, respectively, and a laser/temperature control system (LTC100, Thorlabs). The excitation light, from the laser whose intensity is adjusted appropriately by a variable attenuator (FVA-3100, EXFO, Canada), is coupled into a source fiber with core diameter of 62.5 μm and numerical aperture (NA) of 0.22. Then, the output beam is collimated and impinges the boundary of the phantom. The transmitted light is collected by $D = 8$ detection fibers of 500 μm core diameter and NA = 0.37, evenly distributed from 90° to 270° opposite to the incidence position with their tips being 1 mm apart from the phantom surface, i.e., in a noncontact detection geometry, and coupled into an 8×1 fiber-optic switch with its output collimated again for normal incidence to a successive motorized filter wheel (FW102B, Thorlabs) that houses a bandpass interference filter (Cy5.5-A Emitter, Semrock) with transmission of >93% over the bandwidth from 696 to 736 nm and rejection ratio of OD > 6 outside the passband. The filtered light, finally, enters into a PMT photon-counting head (H7155-01, Hamamatsu, Japan) coupled with a counting unit (C8855, Hamamatsu, Japan) for the photon-counting detection. A 32-bit counter in the counting unit offers a large dynamic range of measurement that eliminates requirement for neutral density filters. The data acquisition is performed for the emission and excitation signals with and without the filter in place, respectively, as well as for dark signals with the PMT fully blocked. By rotating the phantom at an angular interval and translating it at a vertical displacement, three-dimensional (3-D) spatial sampling process can be achieved with a programmed pattern. The whole experimental set is placed in a dark environment to shield the stray light. In our experiments, the integration times of photon-counting unit were set to 100 and 500 ms for the excitation and emission measurements, respectively. 2-D data-set at middle height of the phantom was acquired with an angular interval of 5.625°, which provides $S = 64$ equally spaced projection angles. This leads to two sets of 64×8 measurements at the excitation and emission wavelengths, respectively.

2.2 *Materials*

The pH-sensitive DFT experiments were performed on a rat-sized cylindrical phantom, made from a cylindrical Polyformaldehyde chamber filled with a mixture, also referred to as background solution, of 1%-Intralipid solution and Cy5.5 dye (GE Healthcare) with a concentration of about $C_B = 10$ nM and weak acidity of $\mathrm{pH}_B \approx 6.5$, as shown in Fig. 2. The chamber has an outer radius of $R = 20$ mm, a height of $H = 50$ mm and a wall thickness $d = 2$ mm. The absorption and the reduced scattering coefficients of the background solution were determined to be $\mu_a^{(B)} = 0.0043\ \mathrm{mm}^{-1}$ and $\mu_s'^{(B)} = 0.89\ \mathrm{mm}^{-1}$, respectively, with a time-resolved spectroscopic (TRS) technique,[24] and assumed to be approximately equal at both the excitation and emission wavelengths, while the fluorescent parameters of the background were empirically set to $\eta\mu_a = 1 \times 10^{-8}\ \mathrm{mm}^{-1}$ to be adapt to the difference scheme. To simulate a fluorescent target embedded in tissue, a thin cylindrical tube having an outer radius of $R_t = 5$ mm, a height of $H_t = 30$ mm, and a wall thickness $d_t = 0.5$ mm, consequently, the inner radius of $R_t^{\mathrm{in}} = 4.5$ mm, which is filled with mixture solution of 1%-Inraplipid and Cy5.5 dye with various concentrations and pH-values, was vertically inserted into the background solution, with its center located at ($r = 9$ mm, $\theta = 0°$). The phantom chamber and target tube are both fabricated from polyformaldehyde whose optical properties are determined to $\mu_a = 0.0038\ \mathrm{mm}^{-1}$ and $\mu_s' = 0.978\ \mathrm{mm}^{-1}$ at the excitation wavelength, again by the TRS technique. The distance between the phantom top and the image plane was $H_I = 20$ mm. It has been demonstrated, that the pH-sensitive pentamethine cyanine dyes, such as Cy5.5, have increased fluorescence intensity as their pH-value is decreased.[1,20] Therefore, in the following pH-sensitive DFT experiments, the diluted hydrochloric-acid and aqueous-sodium-hydroxide solution were used to lower and elevate the pH-value of the Cy5.5 target, respectively, while keeping the Cy5.5 concentrations approximately unchanged.

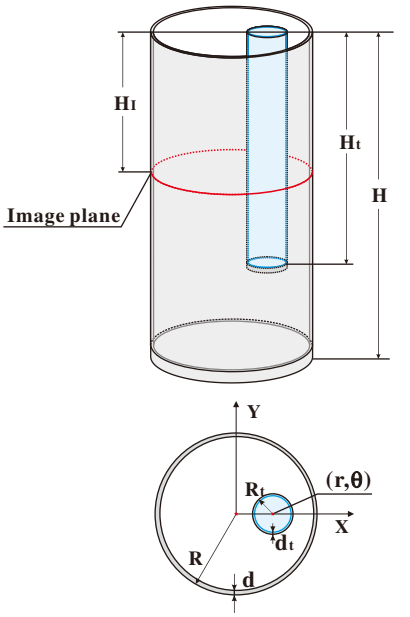

Fig. 2 Sketch of the phantom embedding a fluorescent target used in the experiments.

2.3 *Data-Type*

With a goal of visualizing pH-sensitive variation of fluorescence yield inside turbid medium with enhanced sensitivity, the proposed difference-DFT scheme calculated a normalized Born difference data-type to reduce the influences of system errors on the reconstruction accuracy and the fluorescence baseline on extracting the pH-sensitive signals.[25]

$$\Delta\Gamma_{\mathrm{nb}}(\mathbf{r}_d^{(s)}, \mathbf{r}_s) = \frac{[\Gamma_m^{(T)}(\mathbf{r}_d^{(s)}, \mathbf{r}_s) - \Gamma_m^{(R)}(\mathbf{r}_d^{(s)}, \mathbf{r}_s)]/T_m}{\Gamma_x(\mathbf{r}_d^{(s)}, \mathbf{r}_s)/T_x - \Gamma_d(\mathbf{r}_d^{(s)}, \mathbf{r}_s)/T_d}, \quad (1)$$

where $\mathbf{r}_s$ is the position vector of the s-th source illumination ($s = 1, 2, \ldots, S$) and $\mathbf{r}_d^{(s)}$ the position vector of the d-th detector ($d = 1, 2, \ldots, D$) regarding the s-th source; $\Gamma_m^{(T)}(\mathbf{r}_d^{(s)}, \mathbf{r}_s)$ is the measured emission data, i.e., the outgoing flux in photon counts, at a target pH-status; $\Gamma_m^{(R)}(\mathbf{r}_d^{(s)}, \mathbf{r}_s)$ and $\Gamma_x(\mathbf{r}_d^{(s)}, \mathbf{r}_s)$ are the measured emission and excitation data at a reference pH-status, respectively; $\Gamma_d(\mathbf{r}_d^{(s)}, \mathbf{r}_s)$ is the dark counts; T_m, T_x and T_d are the photon-counting times such as the integration

times, for the emission, excitation and dark measurements, respectively.

2.4 *Difference Image Reconstruction*

For computational simplicity, we employ the mathematically-tractable diffusion (P_1) approximation to the radiative transfer equation (RTE) as the forward model,[16,26] although the RTE is more universal and especially suitable for the whole-body image of small animals.[27,28] In CW-DFT regime, this leads to the following steady-state coupled diffusion equations.[16,25,26]

$$\begin{cases} [\nabla\cdot\kappa_x(\mathbf{r})\nabla-\mu_{ax}(\mathbf{r})c]\mathbf{\Phi}_x(\mathbf{r},\mathbf{r}_s)=-\delta(\mathbf{r}-\mathbf{r}_s) \\ [\nabla\cdot\kappa_m(\mathbf{r})\nabla-\mu_{am}(\mathbf{r})c]\mathbf{\Phi}_m(\mathbf{r},\mathbf{r}_s)=-c\mathbf{\Phi}_x(\mathbf{r},\mathbf{r}_s)\eta(\mathbf{r})\mu_{\mathrm{af}}(\mathbf{r}) \end{cases}, \tag{2}$$

where subscripts x and m denote the excitation and emission wavelengths, respectively; $\mathbf{\Phi}_\nu(\mathbf{r},\mathbf{r}_s)(\nu\in[x,m])$ is the spatially-varying photon density for a source at $\mathbf{r}_s$; $\mu_{a\nu}$ and κ_ν are the absorption and diffusion coefficients at the excitation and emission wavelengths, respectively; $\eta(\mathbf{r})$ and $\mu_{\mathrm{af}}(\mathbf{r})$ denote the quantum-efficiency and absorption coefficient of the fluorescent agent, respectively; c is the light speed in tissue.

Within the framework of the normalized Born formulation, an integral equation that links the measurable normalized Born difference data-type with the unknown difference fluorescence yield, referred to as the difference imaging equation, can be established in terms of Eq. (2).

$$\mathbf{\Phi}_x(\mathbf{r}_d^{(s)},\mathbf{r}_s)\Delta\Gamma_{\mathrm{nb}}(\mathbf{r}_d^{(s)},\mathbf{r}_s)=\int_\Omega cG_m(\mathbf{r}_d^{(s)},\mathbf{r})\mathbf{\Phi}_x(\mathbf{r},\mathbf{r}_s)\Delta y(\mathbf{r})\mathrm{d}\mathbf{r}, \tag{3}$$

where $\Delta y(\mathbf{r})=\eta^{(T)}(\mathbf{r})\mu_{\mathrm{af}}^{(T)}(\mathbf{r})-\eta^{(R)}(\mathbf{r})\mu_{\mathrm{af}}^{(R)}(\mathbf{r})$, with the superscripts T and R indicating the target and reference status, respectively; $\mathbf{\Phi}_x(\mathbf{r}_d^{(s)},\mathbf{r}_s)$ is the model-calculated photon-density for the excitation at $\mathbf{r}_s$ and detection at $\mathbf{r}_d^{(s)}$; $G_m(\mathbf{r}_d^{(s)},\mathbf{r})$ is the Green's function of the emission diffusion equation for the excitation at $\mathbf{r}$ and detection at $\mathbf{r}_d^{(s)}$; $\mathbf{\Phi}_x(\mathbf{r},\mathbf{r}_s)$ is the excitation photon-density at $\mathbf{r}$ for the excitation at $\mathbf{r}_s$; Ω is the volume of interest. It is worth explaining that, although the noncontact detection geometry was employed in the setup, the model predicted flux-regarding quantities that correspond to the measured signals $\Gamma_\nu^{(T)}(\mathbf{r}_d^{(s)},\mathbf{r}_s)$, were approximated by the outgoing flux at the boundary sites closest to the detectors and, therefore, were calculated as the corresponding photon-density-regarding quantities instead in the above Born normalized equation.

To reconstruct the deference-yield, $\Delta y(\mathbf{r})$, Eq. (3) is discretized using a mesh of N elements, leading to an ill-posed matrix equation

$$\Delta\mathbf{\Phi}_m=\mathbf{W}\Delta\mathbf{y}, \tag{4}$$

where $\Delta\mathbf{\Phi}_m$ is a column vector of DS-length, numerating $\mathbf{\Phi}_x(\mathbf{r}_d^{(s)},\mathbf{r}_s)\Delta\Gamma_{\mathrm{nb}}(\mathbf{r}_d^{(s)},\mathbf{r}_s)$ for all the source and detection combinations; $\Delta\mathbf{y}$ is a column vector of N-length, numerating $\Delta y(\mathbf{r})$ at N meshing elements; $\mathbf{W}$ is the DS × N-dimensional sensitivity matrix with its entry calculated as $W(\mathbf{r}_d^{(s)},\mathbf{r}_s,n)=cG_m(\mathbf{r}_d^{(s)},\mathbf{r}_n)\mathbf{\Phi}_x(\mathbf{r}_n,\mathbf{r}_s)\Delta V_n$, where $\mathbf{r}_n$ points at the center of the n-th element and ΔV_n the volume of the n-th element. In a 2-D optically homogenous circular domain, as assumed in this study, $G_m(\mathbf{r}_d^{(s)},\mathbf{r}_n)$, $\mathbf{\Phi}_x(\mathbf{r}_n,\mathbf{r}_s)$ and $\mathbf{\Phi}_x(\mathbf{r}_d^{(s)},\mathbf{r}_s)$ are all the analytical solutions of the diffusion equation on a circular homogeneous domain of 40mm-diameter with the background optical properties under the extrapolated-boundary condition.[29]

An efficient and robust solution to Eq. (4) can be obtained using the randomized algebraic reconstruction technique, whose row-fashioned performance makes the inversion process nearly memory-independent and robust.[21,30] Therefore, it is favorably applicable to inverting an ill-conditioned matrix of large-scale, such as those arising from the 3-D scenarios.

3 Results and Discussions

3.1 *Quantitative Performances*

Prior to the pH-sensitive imaging, we have performed a series of experiments, using the phantom with the fluorescent targets of different concentration, to assess the quantitative accuracy and reliability of the difference image reconstruction method. The concentration of Cy5.5 dye in the target inclusion C_T, was varied in a range from 0 to 20 nM with a step of 2.5 nM while keeping the target pH-value constant, i.e., $\mathrm{pH}_T=6.5$, and the relative concentration ratio of target-to-background, defined as $R^{(C)}=(C_T-C_B)/C_B$, accordingly ranged from −1.0 to 1.0 with a increment of 0.25. To achieve the difference imaging scheme, the reference-status measurement was firstly performed on the homogeneous phantom comprised of only the background solution, $R^{(C)}=0$. Figure 3(a) illustrates the reconstructed difference-yield images and their profiles drawn along the X-axis, also known as the X-profiles, for the above varying dye concentrations. In addition, some artifacts around the detection boundaries and the target can be observed in Fig. 3(a). We believe that this defect is probably caused by difference in the optical properties between the background solution and the phantom chamber as well as target tube, which results in breakdown in the first-order diffusion theory at the interface between the drastically distinct optical regions. Other factors accounting for the artifacts might include the deviation of the experimentally measured optical properties from their true ones, the mismatch between the approximated contact calculation model, and the actual noncontact measurement mode, as well as various kinds of noises in the experimental process. Figure 3(b) depicts the maximum-normalized peak difference-yield reconstructed by the difference-DFT, therefore, the ratio of the reconstructed peak difference-yield in the target region to the absolute value of that for $R^{(C)}=-1$, versus the relative concentration ratio $R^{(C)}$, where an excellent reconstruction fidelity between the original targets and the reconstructed ones is manifested by a linear regression model with a correlation coefficient of $R^2=0.9993$. The minor deviation of the reconstructed quantity from its true value, especially in the case of high concentration of the dye, might be ascribed to the degraded water-solubility of the Cy5.5 agent in that status as well as the measurement noise. The results demonstrate that the proposed difference-DFT method has the capability of quantifying the concentration variation with high accuracy, and in analogy, allows for discerning pH-induced quantum-efficiency variation in turbid medium, by reconstructing the difference-yield distribution, i.e., the pH-sensitive imaging.

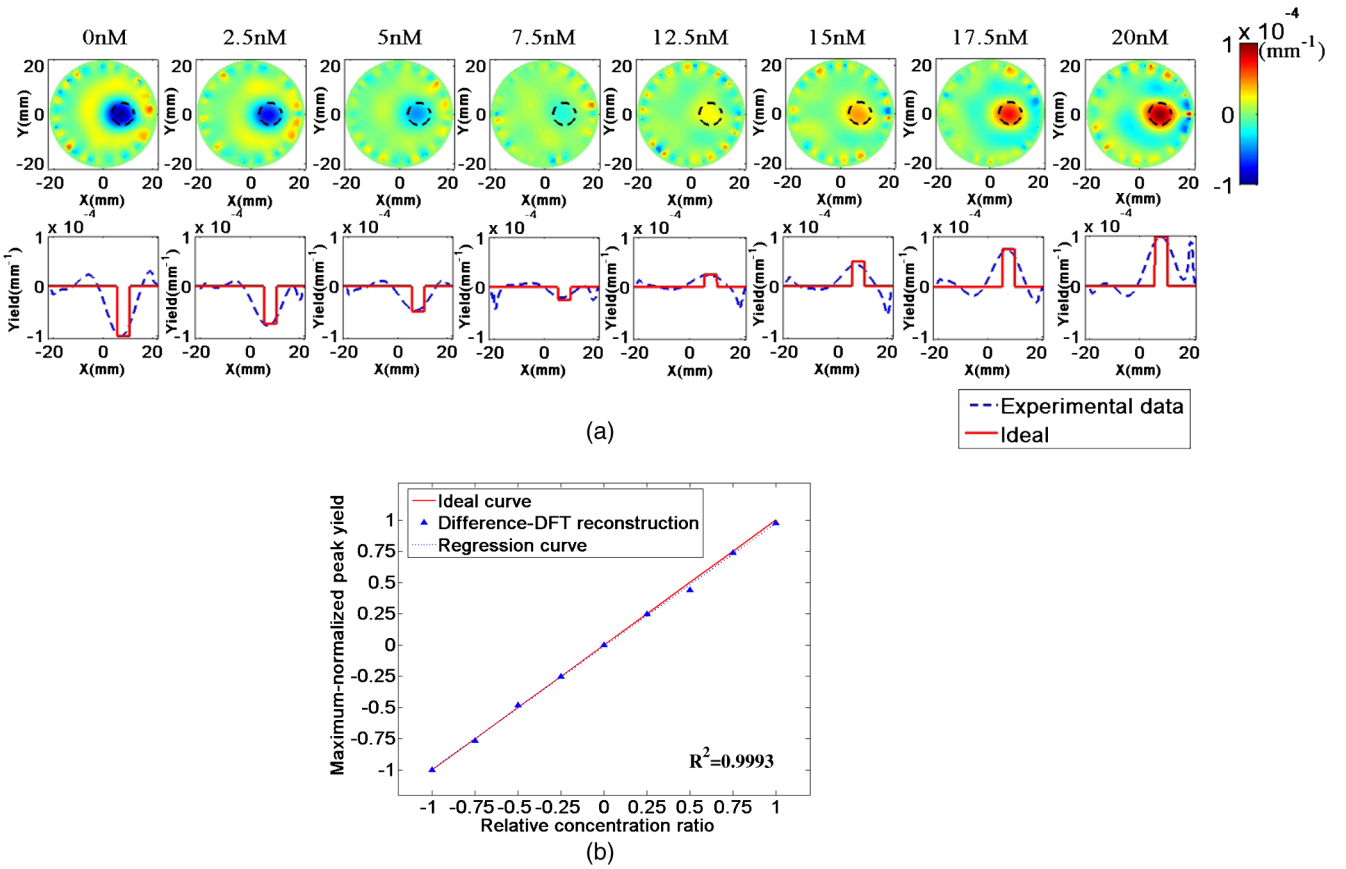

Fig. 3 Phantom experiments with a fluorescent target of the varying dye concentration from 0 to 20 nM to assess the quantitative accuracy and reliability of the difference-DFT method. (a) The reconstructed difference-yield images and their X-profiles, with the dash circle in each image indicating the location and size of the target inclusion. (b) The maximum normalized peak yield reconstructed by the difference-DFT as a function of the relative concentration ratio $R^{(C)}$.

3.2 *pH-Sensitive Resolutions*

For the quantitative assessment of the pH-sensitive imaging potential, we have performed phantom experiments with the fluorescent target having three target-to-background contrasts in concentration of 1:1, 3:1, and 6:1, i.e., $C_T =$ 10 , 30, and 60 nM, respectively. The choice of the concentration contrasts is to emulate the baseline pH-value contrast situations in various stages of cancer development. During very early stages of cancer when the morphological appearance of the cancer vascularization has not yet formed or the cancer is still in the avascular growth period, hypoxic, ischemic and acidic areas can be evident.[31] With the fact that the exogenously injected agents could not accumulate at the cancer region without leaky cancer vasculature, it might be concluded that conventional DFT methods, which aim at reconstructing the fluorescent yield distributions, may be improper for prospective estimations of cancer localization or relevant pharmacokinetics in the stage. In contrast, pH variability of the microcirculation may manifest and, thus, becomes a common feature in the early-stage tumor region.[31]

To investigate the potential of the pH-sensitive imaging in the early tumor stage, the fluorescence target in the first set of the experiments had the same concentration of the Cy 5.5 agent as that of the background solution, *i.e.* $C_T = C_B = 10$ nM, but different target pH-values of 4.0, 4.5, 5.5, 7, 7.5, and 8.0, as measured by a pH meter (FE20, Mettler Toledo, Switzerland). As with the above case, the reference-status measurement was carried out on the homogeneous phantom, which was comprised of only the background solution, $\mathrm{pH}_T = 6.5$. Figure 4(a) and 4(b) illustrate the yield images experimentally reconstructed with the above varying target pH-value and their X-profiles, respectively. The results show that the proposed methodology is able to disclose the position and size of the target with reasonable accuracy, but with the slightly distorted shape that is ascribed to the ill-posed nature of the inverse problem, the measurement noise and the approximated detector modeling in the used noncontact mode. It is observed from the reconstructions, that the yield of the target proportionally varies as its pH-value differs from its baseline pH-value of $\mathrm{pH}_T = 6.5$. This observation is in good agreement with results published in literatures,[20] and demonstrates the potential of the method as a tool of monitoring physiologically and pathologically-related pH-abnormalities during the early cancer stage.

Due to the hastily formed new microvessels arising from neovascularization, a series of morphological and functional abnormalities occur in rapidly growing cancer, such as incomplete endothelial lining, interrupted basement membrane, more severe hypoxia, ischemia and acidosis. Thus, there are some differences in the transportation of fluorescence agents between normal and cancer tissues in this developing stage. The agents would be quickly delivered in tight capillaries of normal vessels and easily excreted from the body through physiological means, such as metabolism, while they may diffuse into or deposit onto

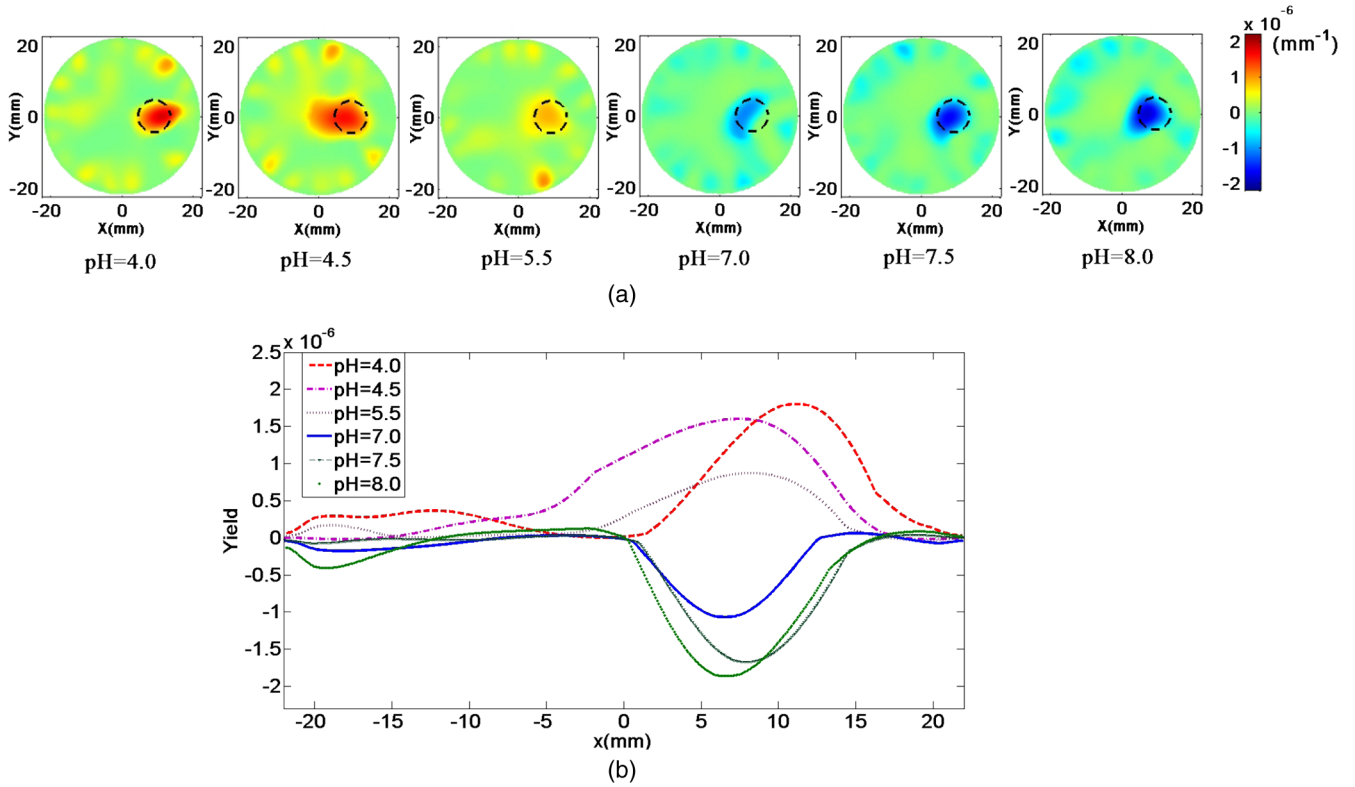

Fig. 4 Phantom experiments with a fluorescent target of target-to-background concentration contrast 1 : 1 and the varying target pH-values for emulating the situations in early tumor stage. (a) The experimentally reconstructed yield images and (b) their X-profiles.

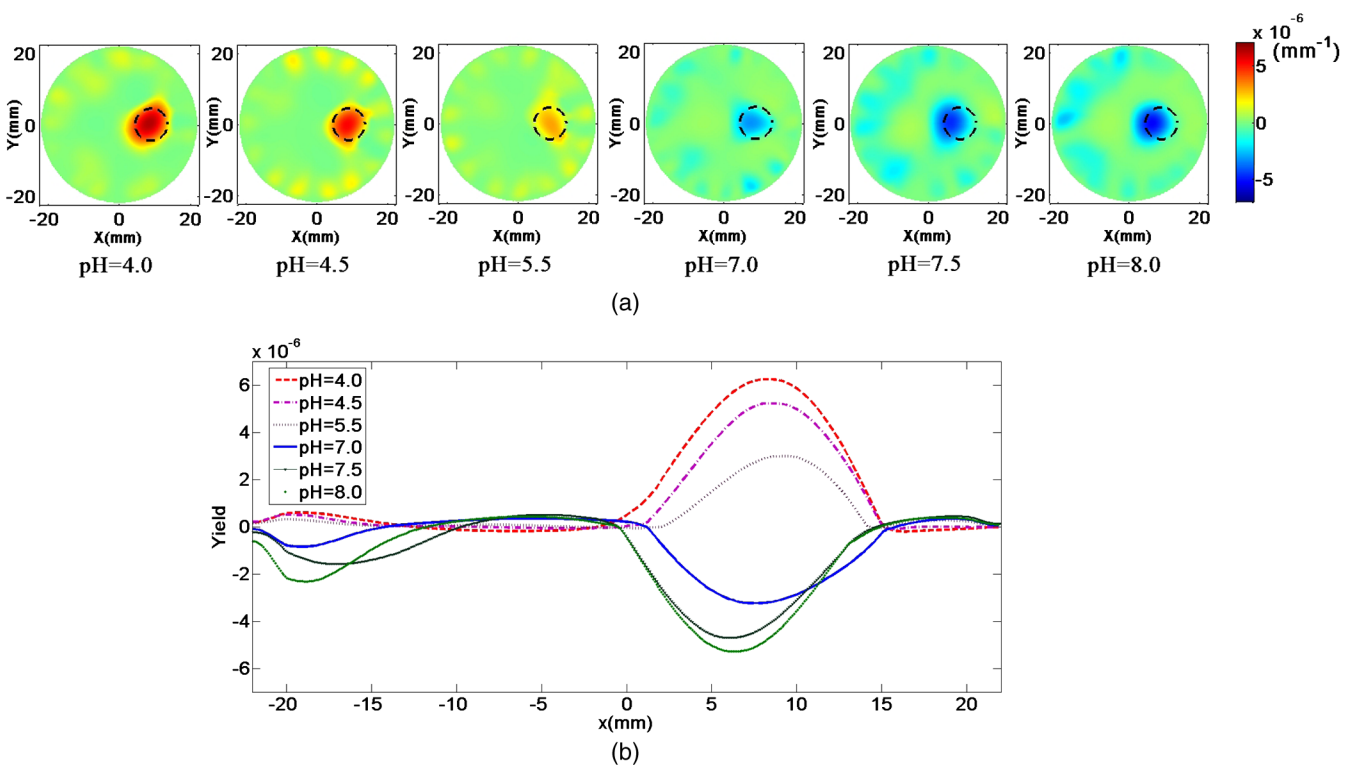

Fig. 5 Phantom experiments with a fluorescent target of target-to-background concentration contrast 3 : 1 and the varying target pH-values to emulate the situations of growing tumors. (a) The experimentally reconstructed yield images and (b) their X-profiles.

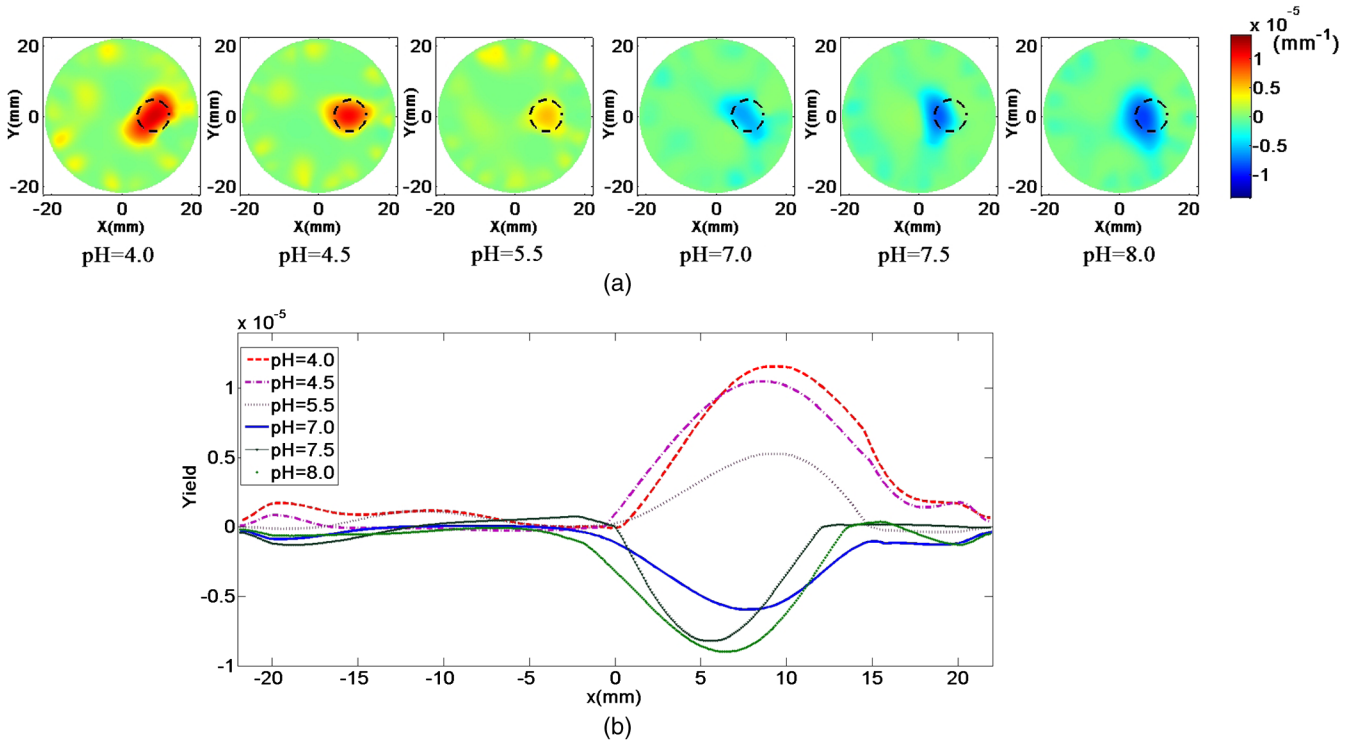

Fig. 6 Phantom experiments with a fluorescent target of target-to-background concentration contrast 6:1 and the varying target pH-values for emulating the situations in late cancerous stage. (a) The experimentally reconstructed yield images and (b) their X-profiles.

the cancer region due to leaky capillary of cancer vessels. Consequently, this leads to a concentration contrast of the agent distribution between normal and cancerous areas. To account for the scenario, we have performed the second set of experiments employing a target-to-background concentration contrast of 3:1, and various target pH-values as the above scenario. Figure 5(a) and 5(b) illustrate the experimentally reconstructed images of the difference-yield at the different target pH-values and their X-profiles, respectively, where the shape, location and yield variation trend of the reconstructed target are closely similar to those in the first set of experiments, except that, in consistency with the 3:1 target-to-background concentration contrast, the reconstructed difference-yields in the target region are approximately three times the corresponding ones in the first experiments.

As malignant tumor grows, both the fluorescence contrast and pH-values would be having even more changes for an increasing vascular permeability and the absence of a functioning lymphatic drainage system in the cancerous region. We have, therefore, designed the third set of experiments with a higher target-to-background concentration contrast of 6:1 and the same pH variations as before for further validation of the method performance in this late cancerous stage. As shown in Fig. 6(a) and 6(b), the experimental results demonstrate that, with the aid of this pH-sensitive fluorescence probe, the proposed method could reconstruct the pH-induced changes in fluorescence yield distribution. Again, it is noted that the difference-yields in the target region were reconstructed in agreement with the used target concentration, which corresponds to approximately two-fold those in the second case.

For better quantifying the correlation of the yield variation trend with the pH change, we define the normalized fluorescence yield as ratio of the reconstructed difference-yield extremum in the target region at a given pH-value $\Delta\hat{y}(\mathrm{pH})$ to that at a specific pH-value of 4.5, $\Delta\hat{y}(\mathrm{pH}=4.5)$, therefore, $R_{\Delta y}(\mathrm{pH}) = \Delta\hat{y}(\mathrm{pH})/\Delta\hat{y}(\mathrm{pH}=4.5)$. According to this definition, the normalized quantity, $R_{\Delta y}$, is equal to unity at pH = 4.5, which was the low limit of the pH-values used in Ref. 20. We have calculated the above normalized quantities as functions of pH-value for the three target concentrations used in the study, and compared the three fitting curves with the fluorescence-intensity counterpart analogously rescaled from Ref. 20, as shown in Fig. 7. It is demonstrated that, despite of the noticeable

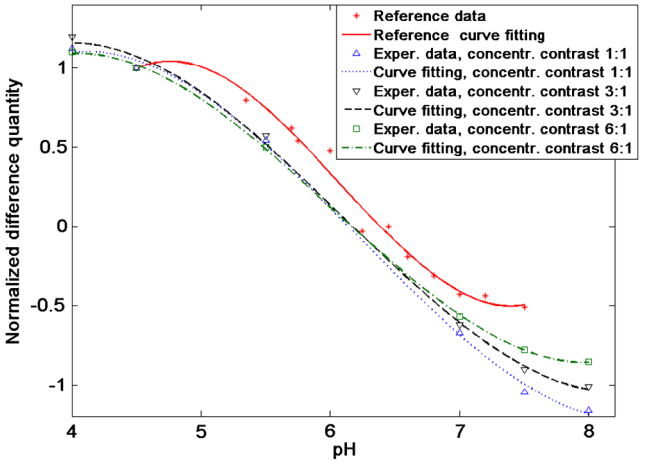

Fig. 7 The normalized quantity (the ratio $R_{\Delta y}(\mathrm{pH})$ of the reconstructed difference-yield extremum in the target region at a given pH-value to that at a specific pH-value of 4.5) and the fitting curves as functions of pH-value for the three target concentrations used in the study and the fluorescence-intensity counterpart analogously rescaled from Ref. 20.

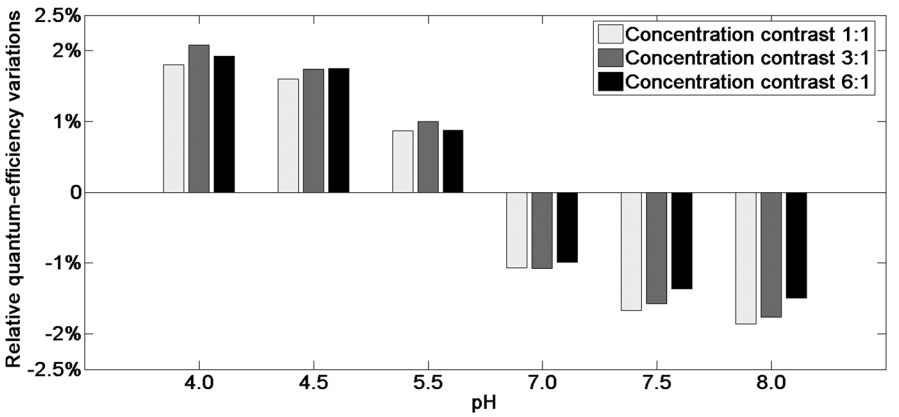

Fig. 8 The relative quantum-efficiency variations of the target as a function of the pH-value, i.e., the ratios of the pH-sensitive difference-yield values to their target yield values.

differences between the measured quantities and the reference ones, the proposed photon-counting difference-DFT scheme could resolve the pH-induced yield variation of a fluorescence probe with high fidelity.

In essence, the pH-induced fluorescence variation is physically due to the alteration of the quantum-efficiency of the agent. Thus, on assumption that the dye concentration is constant, the above normalized yield variation is equivalent to the corresponding relative pH-induced change in the quantum-efficiency. In some practical scenarios, such as in the late phase of the agent dynamics, where the dye concentration in the target regions might be roughly regarded as unchanged due to the slow metabolic process, the relative pH-sensitive variation of the quantum-efficiency can be approximately obtained with a combined difference- and conventional-DFT scheme, where the ratio of the difference-yield acquired with the difference-DFT at the target-status to the absolute-yield reconstructed by the conventional-DFT at the reference-status is calculated as the measure. With the known dye concentrations in the above experiments, Fig. 8 illustrates the relative pH-sensitive quantum-efficiency variations of the target, the ratios of the pH-sensitive difference-yield values to their target yield values calculated with quantum-efficiency at the baseline pH-value, $\eta = 0.23$, as a function of the pH-value for a comparison of the reconstruction accuracy at different target concentrations. The results demonstrate that the reconstruction of the pH-sensitive quantum-efficiency variation is less subject to the dye concentration of the target with the proposed difference-DFT methodology.

Finally, it should be pointed that, although we have just dealt with the CW difference-DFT technique to image pH-sensitive yield variation in the above discussions, the proposed methodology can be readily extended to a TD regime in principle, where it is possible to recover both the pH-induced yield and lifetime variations with a time-correlated-single-photon-counting-based CT-analogous system and an extended generalized-pulse-spectrum-technique-based featured-data image reconstruction scheme.[21,26] This dual-parametric imaging scheme will allow increasingly accurate profiling of the biochemical progressions in cancerous tissues.

4 Conclusions

To investigate the feasibility of quantifying pH-sensitive fluorescence targets in turbid medium, we have presented a difference-DFT methodology for accurately quantitative reconstruction of fluorescent yield in 2-D circular domain. The experimental validations on the rat-sized cylindrical phantom utilize a specifically designed CT-analogous photon-counting system that could achieve the high-speed, ultra-high sensitivity, and dense spatial sampling measurements. We, firstly, experimentally assessed the quantitative performance of the proposed method on a phantom embedding a fluorescent target with different concentrations, and quantitatively validated the nearly linear relationship between the recovered target fluorescent yield changes and the concentration variations. Then, the feasibility and efficacy of the pH-sensitive DFT image have been investigated using three sets of phantom experiments with the fluorescence target of varying pH-values, under different target-to-background concentration contrasts for simulating the situations in various stages of cancer development. The results demonstrate that the proposed difference-DFT scheme might provide a promising alternative to the fluorescence-lifetime imaging method for probing pH-involved pathology and physiology of diseases in some small-animal-based investigations.

Acknowledgments

The authors acknowledge the funding supports from the National Natural Science Foundation of China (30970775, 81101106, 61108081), Chinese National Programs for High Technology Research and Development (2009AA02Z413), Tianjin Municipal Government of China (10JCZDJC17300).

References

1. J. Y. Han and K. Burgess, "Fluorescent indicators for intracellular pH," *Chem. Rev.* **110**(5), 2709–2728 (2010).
2. B. P. Mahoney et al., "Tumor acidity, ion trapping and chemotherapeutics I. Acid pH affects the distribution of chemotherapeutic agents *in vitro*," *Biochem. Pharm.* **66**(7), 1207–1218 (2003).
3. O. A. Andreev et al., "Mechanism and uses of a membrane peptide that targets tumors and other acidic tissues *in vivo*," *Proc. Nat. Acad. Sci.* **104**(19), 7893–7898 (2007).
4. P. Swietach, R. D. Vaughan-Jones, and A. L. Harris, "Regulation of tumor pH and the role of carbonic anhydrase 9," *Cancer Metastasis Rev.* **26**(2), 299–310 (2007).
5. S. Egginton, E. W. Taylor, and J. A. Raven, "Measurement of intracellular pH: a comparison between ion-sensitive microelectrodes and fluorescent dyes," Chapter 1, in *Regulation of Tissue pH in Plants and Animals: A Reappraisal of Current Techniques*, pp. 1–18, Cambridge University, Cambridge, United Kingdom (2004).

6. R. J. Labotika, "Measurement of intracellular pH and deoxyhemoglobin concentration in deoxygenated erythrocytes by phosphorus-31 nuclear magnetic," *Biochemistry* **23**(23), 5549–5555 (1984).
7. J. Slavik, "Applications of fluorescent probes in cellular biology measurement of intracellular pH," *J. Luminescence* **72–74**, 575–577 (1997).
8. D. Ellis and R. C. Thomas, "Microelectrode measurement of the intracellular pH of mammalian heart cells," *Nature* **262**(5565), 224–225 (1976).
9. V. Ntziachristos, "Fluorescence molecular imaging," *Annu. Rev. Biomed. Eng.* **8**, 1–33 (2006).
10. F. Leblond et al., "Toward whole-body optical imaging of rats using single-photon counting fluorescence tomography," *Opt. Lett.* **36**(19), 3723–3725 (2011).
11. V. Ntziachristos et al., "Fluorescence molecular tomography resolves protease activity *in vivo*," *Nature Med.* **8**(7), 757–761 (2002).
12. X. L. Song et al., "Reconstruction for free-space fluorescence tomography using a novel hybrid adaptive finite element algorithm," *Opt. Express* **15**(26), 18300–18317 (2007).
13. A. B. Milstein et al., "Fluorescence optical diffusion tomography," *Appl. Opt.* **42**(16), 3081–3094 (2003).
14. A. B. Milstein et al., "Fluorescence optical diffusion tomography using multiple-frequency data," *J. Opt. Soc. Am. A* **21**(6), 1035–1049 (2004).
15. S. Lam, F. Lesage, and X. Intes, "Time domain fluorescent diffuse optical tomography: analytical expressions," *Opt. Express* **13**(7), 2263–2275 (2005).
16. F. Gao et al., "Simultaneous fluorescence yield and lifetime tomography from time-resolved transmittances of small-animal-sized phantom," *Appl. Opt.* **49**(16), 3163–3172 (2010).
17. A. T. Kumar et al., "Time resolved fluorescence tomography of turbid media based on lifetime contrast," *Opt. Express* **14**(25), 12255–12270 (2006).
18. V. Y. Soloviev et al., "Combined reconstruction of fluorescent and optical parameters using time-resolved data," *Appl. Opt.* **48**(1), 28–36 (2009).
19. F. Leblond et al., "Pre-clinical whole-body fluorescence imaging: review of instruments, methods and applications," *J. Photochem. Photobiol. B Biol.* **98**(1), 77–94 (2010).
20. M. E. Cooper et al., "pH-sensitive cyanine dyes for biological applications," *J. Fluorescence* **12**(3–4), 425–429 (2002).
21. F. Gao et al., "A CT-analogous scheme for time-domain diffuse fluorescence tomography," *J. X-Ray Sci. Tech.* **20**(1), 91–105 (2012).
22. N. Deliolanis et al., "Free-space fluorescence molecular tomography utilizing 360° geometry projections," *Opt. Lett.* **32**(4), 382–384 (2007).
23. D. Kepshire et al., "A microcomputed tomography guided fluorescence tomography system for small animal molecular imaging," *Rev. Sci. Instrum.* **80**(4), 043701 (2009).
24. D. L. Qin et al., "Experimental determination of optical properties in turbid medium by TCSPC technique," *Proc. SPIE* **6434**, 64342E (2007).
25. V. Ntziachristos and R. Weissleder, "Experimental three-dimensional fluorescence reconstruction of diffuse media by use of a normalized Born approximation," *Opt. Lett.* **26**(12), 893–895 (2001).
26. F. Gao, H. J. Zhao, and Y. Yamada, "A linear, featured-data scheme for image reconstruction in time-domain fluorescence molecular tomography," *Opt. Express* **14**(16), 7109–7124 (2006).
27. A. D. Klose, V. Ntziachristos, and A. H. Hielscher, "The inverse source problem based on the radiative transfer equation in optical molecular imaging," *J. Comput. Phys.* **202**(1), 323–345 (2005).
28. D. Gorpas, D. Yova, and K. Politopoulos, "A three-dimensional finite elements approach for the coupled radiative transfer equation and diffusion approximation modeling in fluorescence imaging," *J. Quant. Spec. Rad. Trans.* **111**(4), 553–568 (2010).
29. J. Ripoll et al., "Boundary conditions for light propagation in diffusive media with nonscattering regions," *J. Opt. Soc. Am.* **17**(9), 1671–1681 (2000).
30. S. R. Arridge, "Optical tomography in medical imaging," *Inverse Probl.* **15**(2), 41–93 (1999).
31. P. Vaupel, F. Kallinowski, and P. Okunieff, "Blood flow, oxygen and nutrient supply, and metabolic microenvironment of human tumors: a review," *Cancer Res.* **49**(23), 6449–6465 (1989).